

pubs.acs.org/JPCC Article

Interplay of T_d and 1T' Phases Influencing the Transport Properties of $Mo_xW_{1-x}Te_2$ Weyl Semimetals

Sambit Choudhury, Shailesh Kalal, Rajesh Kumar Ulaganathan, Raman Sankar, and Sanjoy Kr Mahatha*



Cite This: J. Phys. Chem. C 2025, 129, 11407-11416



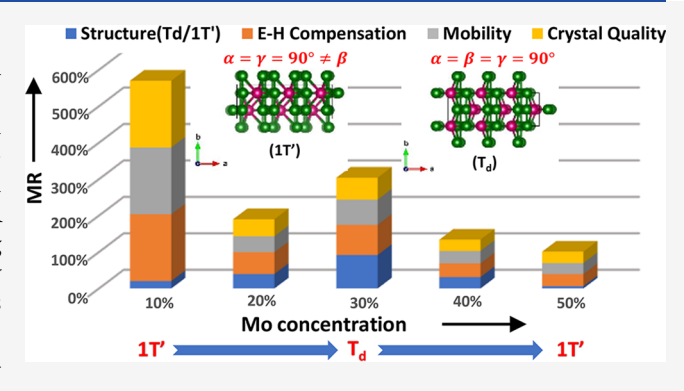
ACCESS I

III Metrics & More

Article Recommendations

s Supporting Information

ABSTRACT: WTe₂ and MoTe₂ in their orthorhombic (T_d) phases have emerged as prominent candidates for type-II Weyl semimetals due to their unique quantum transport phenomena. The distinctive electronic structure leads to unusual electron behavior under a magnetic field, resulting in extreme magnetoresistance (XMR). This study addresses a critical gap in understanding the impact of structural modulation on MR behavior, which has important implications for optimizing materials in quantum devices and spintronics. We successfully synthesized miscible $\text{Mo}_x \text{W}_{1-x} \text{Te}_2$ (x = 0.1 to 0.5) single crystals and investigated their structural evolution and transport properties. Raman and powder XRD analyses reveal that Mo doping induced a transition from the T_d phase to an intermediate monoclinic 1T'



phase. Notably, the x = 0.3 sample exhibits the highest stability toward the $T_{\rm d}$ phase. Transport measurements reveal a significant reduction in MR and residual resistivity ratio (RRR), alongside an increase in electron—hole asymmetry with higher Mo content, attributed to the reduced crystal quality and enhancement of impurity scattering. Enhanced structural stabilization toward the $T_{\rm d}$ phase significantly improves MR and positively influences transport properties. These findings offer new insights into the role of structural tuning in the electronic properties of Weyl semimetals with implications for spintronics and quantum materials research.

INTRODUCTION

Recent advances in low-dimensional quantum materials have significantly broadened the scope of research in areas such as topological insulators, superconductors, and semimetals. Among these, an intriguing class known as Weyl semimetals stands out due to their perfect electron-hole symmetry, exceptionally high electrical conductivity, and remarkable electron mobility. The distinctive electronic structure of Weyl semimetals enables unusual electron behavior when subjected to a magnetic field, often driven by quantum mechanical effects. This behavior results in an exceptional property known as extreme magnetoresistance (XMR), where the material's resistance can increase dramatically ($\sim 10^3$ % at a magnetic field of 9T). To date, a broad class of topological materials, 1-11 exhibiting XMR, has been discovered. The type-II Weyl semimetal candidates WTe2 and MoTe2 have attracted substantial scientific interest and are extensively investigated for XMR, 12-30 due to their intricate electronic structures and unconventional transport mechanisms.

Pristine WTe₂ and MoTe₂ can stabilize into three distinct polytypes under varying experimental conditions: the hexagonal (2H or α phase), the monoclinic (1T' or β phase), and the orthorhombic ($T_{\rm d}$ or γ phase) with space groups $P6_3/mmc$, $P2_1/m$ and $Pmn2_1$, respectively. Out of these phases, the 2H phase exhibits semiconducting characteristics, $T_{\rm d}^{17,36-40}$ while the 1T' and $T_{\rm d}$ phase is reported to be Weyl semi-

metal^{24,25,27,30,41–44} and exhibit XMR effect. Moreover, the 1T' phase of monolayer WTe₂ is reported to exhibit a quantum spin Hall (QSH) state.^{45,46} Significant efforts have been made by researchers to explain the possible mechanisms behind XMR in semimetals,⁴⁷ utilizing transport measurements,^{22,48–51} quantum oscillations,^{23,52–54} and electronic structure ^{19,25,43,55–57} studies.

The XMR mechanism in 1T′-MoTe₂, as well as in WTe₂, has frequently been linked to near-perfect carrier compensation. ^{13,24,43} However, recent studies in MoTe₂²⁵ and WTe₂⁵⁸ indicate that while carrier compensation may be a necessary condition, it alone is insufficient to fully account for XMR in these systems. ⁴³ Additional factors proposed to influence XMR include a high residual resistivity ratio (RRR), ^{12,13,20} high quantum mobility, ^{15,18,53} and strong spin—orbit coupling (SOC). ^{43,56,57} However, no single study has conclusively pinpointed the exact origin of XMR in WTe₂, which remains complex and is not yet fully understood.

Received: March 4, 2025 Revised: May 28, 2025 Accepted: May 29, 2025 Published: June 10, 2025





In addition, miscible single crystals $\mathrm{Mo}_x \mathrm{W}_{1-x} \mathrm{Te}_2$, with different Mo compositions, have been studied to clarify the origin of XMR in WTe₂. 51,53,59 Although XMR effects are somewhat suppressed with Mo doping, $\mathrm{Mo}_x \mathrm{W}_{1-x} \mathrm{Te}_2$ remains a compelling material for multiple reasons. Notably, it hosts novel properties, such as a tunable Fermi-arc Weyl state, $^{60-62}$ pressure-induced superconductivity, 60,61,63 structural phase transitions, $^{62-67}$ and the potential for electronic phase engineering. 62,68 These properties make $\mathrm{Mo}_x \mathrm{W}_{1-x} \mathrm{Te}_2$ an intriguing system for further investigation.

In this study, we systematically conducted XRD and Raman spectroscopy measurements to characterize the various phases present in miscible $\mathrm{Mo_xW_{1-x}Te_2}$ single crystals. Additionally, we performed transport measurements, and a substantial effort has been given to explain the transport properties of these materials in relation to their respective structures. Our analysis of the magnetic-field-dependent MR and temperature-dependent resistivity reveals that Mo doping introduces key changes. Specifically, the increasing asymmetry in electron—hole concentrations, decreasing crystal quality (low RRR value), and the emergence of the 1T' phase contribute to a reduction in MR in Mo-doped WTe₂.

EXPERIMENTAL DETAILS

All preparation steps preceding the quartz tube evacuation and flame sealing were conducted in an argon-filled glovebox, maintaining oxygen and water levels below approximately 1 ppm. Polycrystalline samples were synthesized via a solid-state reaction within evacuated quartz tubes. Stoichiometric mixtures of powdered Mo (purity 99.99%), W (purity 99.99%), and Te (purity 99.999%) were heated at temperatures ranging from 1050 to 1100 °C for 24 h. The samples were then allowed to cool to room temperature over 6 h. The resulting products were ground, pelletized, and subjected to annealing at 1100 °C for 24 h. A custom-designed three-zone muffle furnace, optimized for this process, featured tailored temperature profiles suitable for the growth of single crystals of Mo_xW_{1-x}Te₂. To prepare the materials, a stoichiometric amount of Mo or W/Te at a 1:2 molar ratio (5N purity for Te and 4N purity for Mo) was sealed in an evacuated quartz ampule and heated at 800 °C for 48 h. Approximately 10 g of pre-reacted Mo_{1-x}W_xTe₂ powder was combined with a variable quantity of TeBr₄ (purity 4N, approximately 120 mg) and placed at one end of a silica ampule (40 cm in length with an inner diameter of 1.8 cm and outer diameter of 2.0 cm). The TeBr₄ decomposed to yield bromine concentrations of 2-4 mg, derived from 7 mg of TeBr₄ per cm³, facilitating high transport rates of nearly 150 mg/day. After being annealed, the samples were water-quenched to ambient conditions. The resulting crystals were characterized using energy-dispersive Xray spectroscopy (EDS) conducted on an FEI Quanta 200 FEG environmental scanning electron microscope (SEM). The growth direction of the crystals was confirmed using out-ofplane X-ray diffraction (XRD) measurements performed on a D8 Advance diffractometer with Cu K_{α} irradiation (λ = 1.54060Å), operating at 40 kV and 100 mA. The transport measurements were performed using the four-probe method in a Quantum Design 16 T Physical Property Measurement System (PPMS) (Quantum Design, USA), under controlled temperature (2-300 K) and magnetic field (up to 16 T) conditions. Phase identification was carried out using synchrotron-based XRD and Raman spectroscopy measurements. The XRD measurements were performed for the finely

powdered crystals using a Bruker D8 VENTURE instrument at the EH2 station of beamline P24 at PETRA III, DESY, Germany, utilizing a synchrotron radiation source with a wavelength of 0.5 Å. Raman spectra were obtained using Horiba JY HR-800, a micro-Raman spectrometer equipped with a 473 nm excitation laser and having an overall spectral resolution of \sim 1 cm⁻¹.

■ RESULTS AND DISCUSSION

Microstructural Analysis. To investigate the structural and chemical uniformities, we performed scanning electron microscopy (SEM) and energy-dispersive X-ray spectroscopy (EDS) on $Mo_xW_{1-x}Te_2$ samples (x=0.1-0.5). The SEM images, along with elemental EDS mappings for all as-grown $Mo_xW_{1-x}Te_2$ samples (x=0.1-0.5), demonstrate that the distribution of the elements Mo, W, and Te throughout each sample is uniform (Figure S1). This homogeneity is essential for consistent material properties. Additionally, the EDS spectra, presented in Figure S2, reveal characteristic peaks of Mo, W, and Te, validating the composition and quantitative analysis, detailed in Table 1, demonstrate close agreement with the intended stoichiometry for each respective sample.

Table 1. EDS Results for All Samples

		atomic %	
samples	Mo	W	Te
$Mo_{0.1}W_{0.9}Te_2$	5.60	27.40	67.00
$Mo_{0.2}W_{0.8}Te_2$	8.75	23.85	67.40
$Mo_{0.3}W_{0.7}Te_2$	11.93	19.31	68.76
$Mo_{0.4}W_{0.6}Te_2$	12.71	18.62	68.66
$Mo_{0.5}W_{0.5}Te_2$	16.60	15.63	67.77

X-ray Diffraction. Figure 1a shows an image of as-grown crystals obtained directly after synthesis without further treatment. In contrast, Figure 1b compares the structural configurations of the 1T' and T_d phases. The T_d phase represents the orthorhombic structure, whereas the $1T^{\prime}$ phase is a distorted version of the T_d , with a slight variation in angle β , which impacts the lattice symmetry. We investigated the evolution of the crystal structure in Weyl semimetal Mo-doped WTe₂ by using X-ray diffraction (XRD) measurements. The study aims to resolve subtle structural distinctions between all compositions (x = 0.1 to 0.5) and to understand the impact of doping on lattice parameters. The XRD patterns of the asgrown crystals, shown in Figure 1c, reveal that all observed peaks are indexed as $(0\ 0\ 2k)$ reflections, indicating preferential growth along the c-axis. The full width at half-maximum (fwhm) of the (002) peak ranges between 0.05° and 0.08°, demonstrating the high crystalline quality of the grown samples. With increasing Mo doping, the peaks shift toward higher 2θ angles, consistent with lattice contraction due to the substitution of smaller Mo4+ ions (ionic radius: 65 pm) for larger W4+ ions (66 pm). Furthermore, Le Bail refinement of the XRD patterns of powdered crystals was used for all compositions (x = 0.1 to 0.5) (Figures 1e and S3) to extract the lattice parameters along with the angle β . This analysis indicates that all samples are stabilized in the intermediate phases of T_d and 1T'. As shown in Figure 1f, a notable trend in the β angle shows a minimum value at x = 0.3, suggesting that the crystal structure stabilizes more strongly toward the T_d phase. Our results differ significantly from those reported by Lv

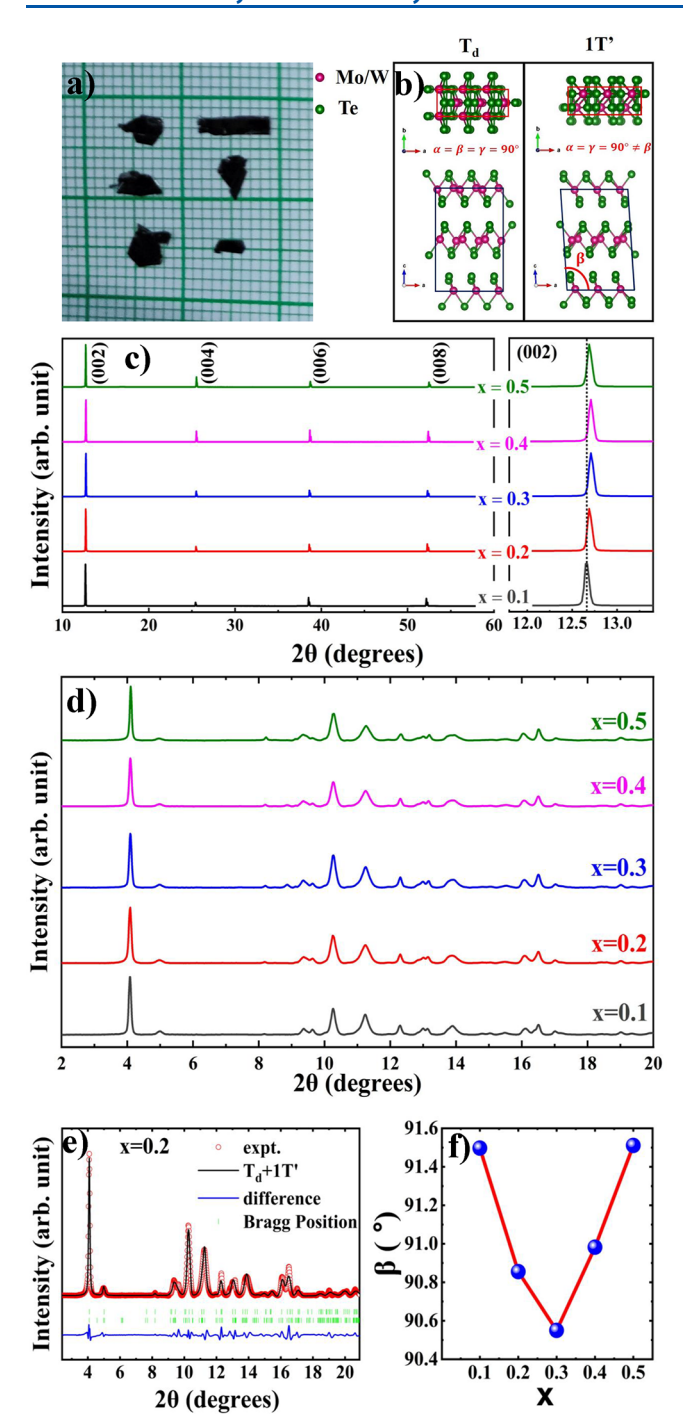


Figure 1. (a) Image of $Mo_xW_{1-x}Te_2$ single crystals grown by the chemical vapor transport method. (b) Crystal structure of $Mo_xW_{1-x}Te_2$ in the T_d and 1T' phases, respectively. (c) XRD patterns of representative $Mo_xW_{1-x}Te_2$ (x=0.1 to 0.5) single crystals. (d) XRD patterns of powdered $Mo_xW_{1-x}Te_2$ (x=0.1 to 0.5) single crystals. (e) Le Bail refinement of powdered $Mo_{0.2}W_{0.8}Te_2$ single crystals, fitted using a dual-phase model (T_d and T_d). (f) Variation of the angle θ with the Mo concentration.

et al., ⁶⁵ where a smooth transition was observed from the $T_{\rm d}$ to the 1T' phase. In contrast, our findings exhibit a different transition behavior, primarily due to precise control over temperature stabilization during crystal growth. Two additional peaks at 2θ values of approximately 4.8 and 8° may be arising from the WO₃ impurity phase. This phase likely results from partial oxidation during the mechanical grinding process. ¹¹

The introduction of oxygen or localized heating during the grinding process can lead to the oxidation of tungsten, forming WO₃. While this impurity phase is a byproduct of sample preparation, it does not significantly affect the conclusions regarding the primary structural evolution with doping as well as the transport mechanism.

Raman Spectroscopy. According to recent studies, 65,66 the crystal structures of $Mo_xW_{1-x}Te_2$ are classified into four distinct domains based on composition: x=0-0.1, x=0.1-0.5, x=0.5-0.7, and x=0.7-1, corresponding to the T_d , mixed $(1T'+T_d)$, 1T' and 2H phases, respectively. Raman spectroscopy was performed for all Mo substitution levels (x=0.1-0.5) of our samples at room temperature to identify the phases. The unpolarized Raman spectra from the ab plane of the as-grown $Mo_{1-x}W_xTe_2$ single crystals, normalized for comparison, are presented in Figure 2. The evolution of

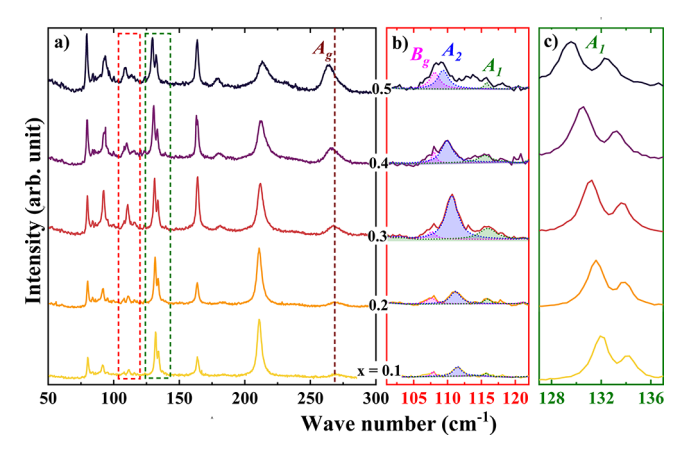


Figure 2. Raman spectra of $Mo_xW_{1-x}Te_2$ single crystals (x = 0.1 to 0.5), showing vibrational modes in different regions (a) 50–300 cm⁻¹, (b) 101-122 cm⁻¹ (with B_g (magenta shade), A_2 (blue shade), A_1 (green shade) modes), and (c) 127-137 cm⁻¹.

composition-dependent structural phases in Mo_xW_{1-x}Te₂ was analyzed by comparing the experimental Raman spectra with theoretical DFT calculations for 1T'-MoTe₂, 1T'-WTe₂, $T_{\rm d}$ -MoTe₂, and $T_{\rm d}$ -WTe₂. 65,66,69 From this analysis, it is inferred that for composition x = 0.1-0.5, the sharp peaks at 80.31, 111.5, 116, 131.96, 134.23, 163.91, and 211.13 cm⁻¹ correspond to the A_1 and A_2 symmetry modes in the $T_{
m d}$ phase. The absence of characteristic A_{1g} (171.89 cm⁻¹) and E_{2g} (230.043 cm⁻¹) modes rules out the possibility of a 2H phase, while the well-split A_1 (~130 cm⁻¹) mode (Figure 2c) confirms the T_d phase in all grown crystals. In the range of 105–120 cm⁻¹(Figure 2b), the superposition of multiple peaks is deconvoluted into three distinct Lorentzian peaks at 107.9, 111.5, and 116 cm⁻¹, consistently observed across all samples. The 107.9 cm⁻¹ peak corresponds to the B_g mode of the 1T'-MoTe₂ phase, while the 111.5 and 116 cm⁻¹ peaks correspond to the A_2 and A_1 modes, respectively, of the T_d phase of $MoTe_2/WTe_2$. The intensity of the B_g mode increases consistently with increasing Mo content. In contrast, the intensities of the A_2 and A_1 modes increase up to x = 0.3, where they reach a maximum and then decrease, while exhibiting redshifts with higher Mo content. This behavior suggests a structural preference of 1T' lattice transitioning to the $T_{\rm d}$ driven by a reduction in the bond angle β to 90° with increasing Mo content up to 30%. The sample at x = 0.3exhibits the most stabilized $T_{\rm d}$ phase, likely due to the optimal

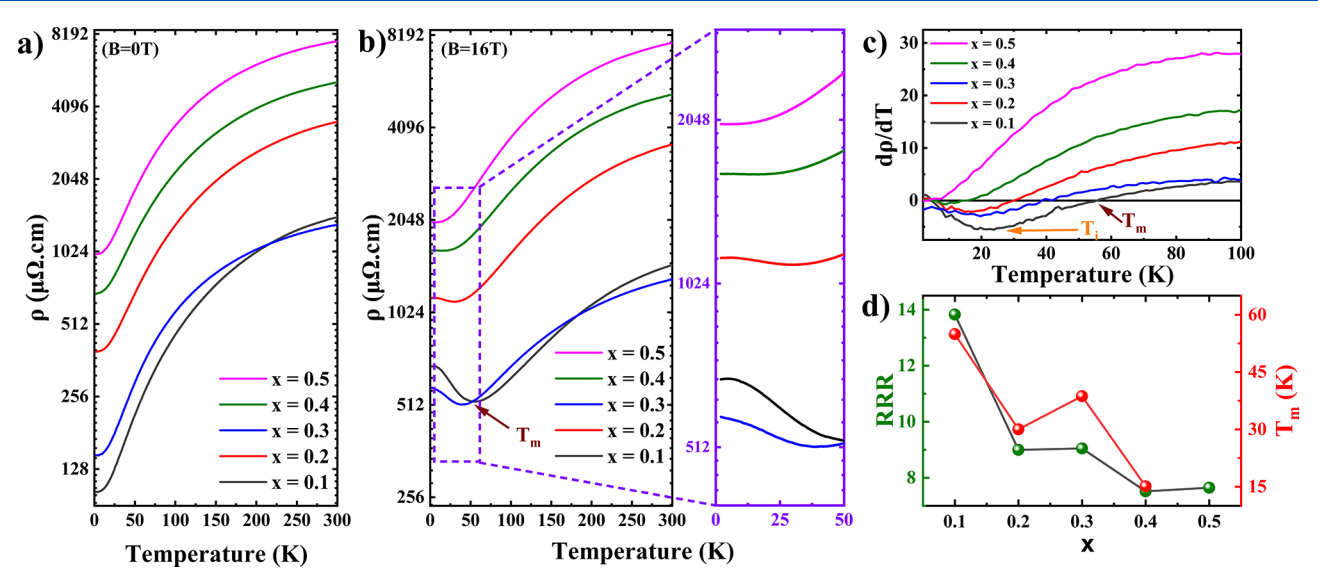


Figure 3. (a) Zero-field temperature dependent resistivity $\rho_{xx}(T)$, (b) temperature dependent resistivity $\rho_{xx}(T)$ at 16T (the right panel shows a zoomed-in view of the data in the 0–50 K range highlighting saturation of the resistivity curve down to T_i). (c) Residual resistivity ratio (RRR) as a function of Mo-substituting level x in the absence of the magnetic field and (d) first-order temperature derivative of resistivity $\frac{d\rho}{dT}$ vs temperature plot at 16T of Mo_xW_{1-x}Te₂ (x = 0.1, 0.2, 0.3, 0.4 and 0.5) single crystals.

stoichiometric balance of Mo and W, which results in an enhanced intensity of the A_1 and A_2 vibrational modes. These modes, characteristic of the 1T'-MoTe₂ lattice, become more prominent in the T_d phase. Additionally, the broadened peak near 270.34 cm⁻¹ is assigned to the A_g mode of the 1T'structure. Interestingly, the intensity of the A_g mode gradually increased with increasing x, attributed to enhanced Raman scattering caused by the loss of translational symmetry due to the random substitution of Mo for W. This substitution disrupts lattice periodicity and increases the fraction of the 1T' phase compared to that of the $T_{\rm d}$ phase. The compositional disorder broadens and intensifies Raman peaks, particularly those sensitive to local bonding environments. From x = 0.1, it systematically redshifts to 264.72 cm⁻¹ as the Mo doping level increases to x = 0.5. This systematic shift implies that introducing Mo introduces lattice strain or disorder that leads to phonon softening. Additionally, increased electron-phonon coupling and the shift in lattice symmetry with the Mo content may contribute to these changes. The asymmetric Raman line shape observed for the peak at 211 cm⁻¹ broadens with increasing Mo substitution, thanks to a reduction in the phonon correlation length (L_c) with decreasing W content.⁶⁶

Resistivity. Figure 3a depicts the temperature-dependent longitudinal resistivity of $Mo_xW_{1-x}Te_2$ (x = 0.1 to 0.5) single crystals in the absence of a magnetic field. The curve illustrates a consistent increase in resistivity across all samples as the temperature varies from 2 to 300 K, signifying the typical metallic behavior. It can also be observed that as the concentration of Mo increases, there is a notable reduction in the RRR value (Figure 3d). Higher doping levels of Mo in WTe2 introduce greater asymmetry in the crystal structure, which is already well-explained by Raman spectroscopy. Additionally, this doping leads to an increase in the number of crystal defects, resulting in enhanced impurity scattering. Notably, an exceptional behavior is observed in the case of Mo_{0.3}W_{0.7}Te₂, which has an RRR of 8.99, greater than that of Mo_{0.2}W_{0.8}Te₂. Generally, the crystalline quality of a crystal is reflected in a good RRR value. This suggests that Mo_{0.3}W_{0.7}Te₂

possesses a higher crystalline quality compared to the other samples, except Mo_{0.1}W_{0.9}Te₂. The maximum RRR of 13.6 at zero field is obtained for Mo_{0.1}W_{0.9}Te₂. The RRR value is quite reduced on Mo-substitution as compared to previously reported WTe2. 13 The RRR values of Mo0.1 W0.9 Te2, $Mo_{0.2}W_{0.8}Te_2$, and $Mo_{0.3}W_{0.7}Te_2$ are quite comparable with the values reported by Lv et al.⁵⁹ Another important observation is that after the application of a strong magnetic field of 16 T parallel to the c-axis, all samples display a resistivity minimum around 50 K and lower (Figure 3b). The crossover from metallic to insulating behavior under high magnetic fields exhibits qualitatively similar characteristics across various semimetals. 27,70,71 Similar behavior, characterized by magnetic field-driven resistivity turn-on, has been reported in recent reports of WTe₂. ^{12,13,15,20-22,48,52} This turnon behavior is attributed to temperature-induced changes in the Fermi surface and the emergence of a high-density-of-states band that may dominate conduction at higher temperatures.¹⁹ The low-temperature resistivity saturation observed in other reported topological materials may result from the contribution of 2D surface states, where surface conduction dominates bulk transport, or from some form of symmetry breaking in the material.7

To identify the two distinct characteristic temperatures, first, the temperatures $(T_{\rm m})$ at which the resistivity minima occur and second, the temperatures $(T_{\rm i})$ at which ${\rm d}\rho/{\rm d}T$ curves exhibit minima, marking the onset of the resistivity upturn and plateau, the temperature derivative of the resistivity curve for all samples are obtained, as illustrated in Figure 3c. It is observed that as the low-Z element Mo substitutes for the high-Z element W (which significantly influences the electronic band structure through spin—orbit coupling (SOC)), the characteristic temperatures $T_{\rm i}$ and $T_{\rm m}$ decrease notably. Ultimately, when 50% of the W atoms are replaced by Mo, there is almost no change in resistivity in response to the applied field. This indicates that SOC in the electronic structure of WTe₂ plays a significant role in the origin of MR.⁴³ Interestingly, an exception is observed with Mo_{0.3}W_{0.7}Te₂,

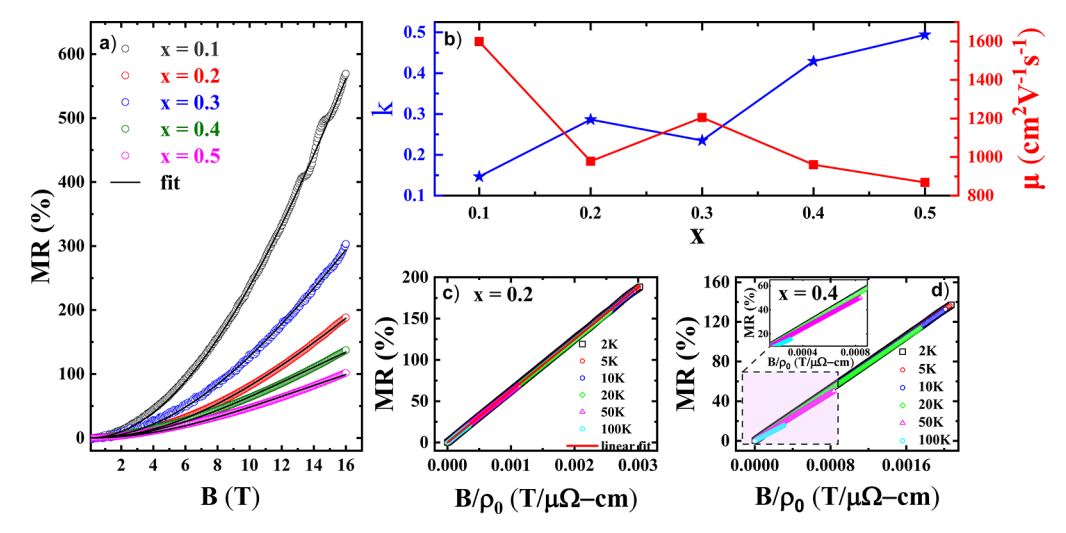


Figure 4. (a) Relationship between MR and magnetic field of $Mo_xW_{1-x}Te_2$ (x=0.1,0.2,0.3,0.4 and 0.5) single crystal at 2 K with magnetic field applied along the c-axis and scanned from 0 to 16 T fitted with the equation $MR = \frac{1+\mu^2B^2}{1+k^2\mu^2B^2} - 1$. (b) Electron-hole concentration asymmetry factor k as a function of Mo-substituting level x. (c, d) Kohler scaling of field dependent MR of stoichiometric $Mo_xW_{1-x}Te_2$ (c) for x=0.2 (the red solid line represents a fit to $MR = 177 \left[\frac{B}{\rho_0}\right]^{1.81}$) and (d) for x=0.4 at distinct temperatures (the inset showing the violation of Kohler's rule for the composition with x=0.4 beyond 50 K).

which exhibits higher T_m and T_i values compared to Mo_{0.2}W_{0.8}Te₂ and shows greater electronic transport sensitivity to the magnetic field. This could be attributed to its superior crystalline quality and unique crystal structure relative to other higher Mo concentration derivatives. Furthermore, the influence of magnetic fields on the spin-orbit coupling (SOC) driven Fermi surface (FS) of WTe₂ has been reported by Rhodes et al.,⁵⁶ where the work demonstrated that the electronic structure of WTe2 is modified under the influence of a magnetic field through Zeeman splitting. The spin-orbit coupled FS can be slightly altered by the Zeeman effect, which appears to shift the spin-dependent density of states at the Fermi level toward van Hove singularities. If a strong magnetic field alters the FS, it is expected to significantly affect the quasiparticle scattering rates and lifetimes. The occurrence of resistivity minima may be ascribed to a field-induced semimetal-to-insulator transition (SMIT), which is proposed to arise from the opening of an excitonic gap in the quasiparticle spectrum. This phenomenon closely mirrors dynamical chiral symmetry breaking seen in relativistic theories of 2 + 1-dimensional Dirac Fermions, which leads to the formation of site-centered charge density waves (CDW). 12 Alternative mechanisms for the semimetal-insulator transition (SMIT) suggest the emergence of superconducting correlations in the domains of Landau level quantization.

Magnetoresistance. The magnetotransport properties of stoichiometric $Mo_xW_{1-x}Te_2$ crystals were investigated to establish a reference for understanding how Mo substitution affects the MR behavior, providing insights into the transport mechanisms and facilitating a comparison with modified compositions. We define magnetoresistance (MR) as

$$MR(\%) = \frac{\rho_{xx}(B) - \rho_{xx}(0)}{\rho_{xx}(0)} \times 100\%$$
 (1)

where $\rho_{xx}(0)$ and $\rho_{xx}(B)$ are the longitudinal resistivity in the absence of the magnetic field and under an applied magnetic field B, respectively. Figure 4a shows the MR curves as a

function of the external magnetic field applied along the c-axis for all samples, measured from 0 to 16 T at 2 K. It can be observed that among all derivatives, the highest MR is achieved for the sample with x=0.1 and with increasing Mo concentration there is a significant decrease of MR value. The observed MR is quietly suppressed in comparison to the previously reported pristine WTe₂. $^{12-14,16,20-23,51,59,75}$

The lowest MR is observed when Mo atoms replace half of the W atoms. Density functional theory (DFT) calculations by Jiang et al. 37 suggest that the spin texture in WTe₂ may prevent backscattering, directly impacting resistivity. This implies that spin-orbit coupling, along with the associated spin and orbital angular momentum textures, could play a significant role in the anomalously large magnetoresistance observed in WTe2. Therefore, it can be inferred that Mo doping may lead to a significant reduction in magnetoresistance, likely due to alterations in the spin and angular momentum textures of pristine WTe2. Notably, the MR of stoichiometric $Mo_xW_{1-x}Te_2$ does not follow a sequential trend with increasing Mo concentration. Specifically, the sample with x = 0.3 exhibits an unusual behavior, showing higher MR values than the sample with x = 0.8, despite the expected trend of MR decreasing with greater Mo substitution. The anomaly observed in the sample with x = 0.3 is likely due to improved crystalline quality and more stability toward the T_d phase, resulting in higher carrier mobility.

To investigate the asymmetry in electron—hole concentration and its impact on average carrier mobility, we employ the two-band model that incorporates contributions from both electrons and holes, with the MR given by

$$MR = \frac{(\mu_{e}|n_{e}| + \mu_{h}n_{h})^{2} + (\mu_{e}|n_{e}| + \mu_{h}n_{h})(\mu_{e}n_{h} + \mu_{h}|n_{e}|)\mu_{e}\mu_{h}B^{2}}{(\mu_{e}|n_{e}| + \mu_{h}n_{h})^{2} + (n_{h} - |n_{e}|)^{2}\mu_{e}^{2}\mu_{h}^{2}B^{2}} - 1$$
(2)

where $\mu_{\rm e}$ and $\mu_{\rm h}$ are the electron and hole mobilities, and $n_{\rm e}$ and $n_{\rm h}$ are the electron and hole concentrations, respectively. By adopting the methods of Lv et al., ⁵⁹ the degree of mismatch between electron and hole concentrations is characterized by the electron—hole concentration asymmetry factor k, which is defined as follows.

$$k = \left| \frac{|n_{\rm e}| - n_{\rm h}}{|n_{\rm e}| + n_{\rm h}} \right| \tag{3}$$

By considering the approximation that the electron and hole mobilities are equal (commonly used to describe MR in semimetals ⁷⁶) i.e., $\mu_{\rm e} = \mu_{\rm h} = \mu$ (μ is the average mobility) the eq 2 can be simplified as

$$MR = \frac{1 + \mu^2 B^2}{1 + k^2 \mu^2 B^2} - 1 \tag{4}$$

Using this model, the MR curves for all compositions were fitted (Figure 4a), and both the average mobilities and the electron—hole concentration asymmetry factor k were extracted, as presented in Table S3. These values align closely with those reported previously by Lv et al. Figure 4b shows that increasing Mo substitution for W atoms leads to a greater imbalance in electron—hole concentrations, as reflected by the increasing k values. Notably, k for the sample with k = 0.3 is slightly lower than that for k = 0.4, suggesting that crystal quality also influences carrier concentration in k Mo_k W_{k-k} The highest average mobility, k 1599.1 cm^k V^{k-k} s^k, is observed for k = 0.1, indicating that mobility may be compromised at higher Mo content.

Further, to gain deeper insights into the scattering mechanisms affecting charge carriers, we employ Kohler's scaling rule, which provides a framework for understanding how MR scales with magnetic field and resistivity. ^{21,50,77,78} According to semiclassical band theory, Kohler's rule can be expressed as

$$MR = \alpha \left(\frac{B}{\rho_0}\right)^m \tag{5}$$

where the parameters α and m are predetermined constants and ρ_0 is the zero field resistivity. According to Kohler's scaling rule, the transverse MR data can be plotted as a function of B/ ρ_0 at various temperatures, as shown in Figures S4 and 4c,d. Ideally, Kohler's rule predicts that if the scattering mechanisms affecting charge carriers remain consistent across all temperatures, the MR curves for different temperatures should converge onto a single, universal curve. Up to 100 K, the samples with x = 0.1 and x = 0.2 show a consistent collapse of their MR curves onto a single curve, indicating similar scattering mechanisms (see Figures S4 and 4c). However, with increased Mo substitution, specifically at x = 0.3, the MR curves begin to diverge from the higher temperature end (see Figures 4d and S4). This inconsistency suggests that for samples with x = 0.3, the scattering mechanism deviates from a uniform behavior, indicating a breakdown in the Kohler scaling at elevated temperatures due to altered scattering processes associated with increased Mo level. On top of that, different scattering processes are active at higher temperatures, such as additional phonon scattering or impurity scattering, which affect carrier dynamics in a manner that is dependent on both temperature and magnetic field. To determine the corresponding α and m values, the distinct MR curves, after applying

Kohler scaling for all temperatures up to 100 K, are fitted using eq 5, (Figure 4a) and are summarized in Table S4. Remarkably, an increase in the Mo content is associated with a decrease in the value of m. This trend provides additional evidence that higher Mo substitution negatively impacts MR, suggesting a reduction in the efficiency of the scattering mechanisms that govern charge carrier dynamics in the material.

The early discovery of WTe2 and MoTe2 as XMR materials highlighted various transport mechanisms underlying their behavior. The report by Zhong et al. 28 revealed that reducing the flake thickness of MoTe₂ decreases both electron and hole densities, and thereby increases the electron-hole imbalance, stabilizing the material in the $T_{\rm d}$ phase. Additionally, a recent study by Akhanda et al. ⁷⁹ reported that the substitution of W atoms in MoTe2 increases the electron concentration by lowering the size of hole pockets, as the W content in the material becomes more electron-dominant. Based on these observations, in our samples, the addition of Mo to WTe2 results in a more hole-dominant character and significantly enhances charge carrier imbalance. For the configuration $Mo_{0.3}W_{0.7}Te_2$, the transition of the 1T' unit cell to the T_d phase induces band structure modifications, leading to a reduction in electron and hole densities along with a substantial increase in charge carrier imbalance. However, crystal quality enhances carrier mobility by minimizing phase boundary scattering, which counteracts the impact of increased electron-hole concentration asymmetry and ultimately improves the MR. Moreover, Mo substitution predominantly alters the scattering mechanisms within the material, shifting the balance from phonon-dominated scattering to impurity scattering. This change significantly modifies carrier dynamics, particularly at elevated temperatures, by introducing additional scattering centers and altering the electronic band structure.

Although the Mo_xW_{1-x}Te₂ system has been widely studied for its structural transitions and MR behavior, 53,59 several key aspects remain unexplored. We investigated compositions with Mo doping from x = 0.1 to 0.5, a range predicted to host tunable Fermi arc surface states characteristic of Weyl semimetals.⁶⁰ This doping regime reveals nonlinear MR behavior and a pronounced anomaly at x = 0.3, which we attribute to structural correlation as confirmed by Raman spectroscopy and Le Bail analysis of powder XRD data, enabling a refined understanding of lattice evolution and phase coexistence not reported in earlier studies. Together, these results strengthen the link between structural and electronic responses and highlight a promising route for tailoring the topological properties in transition metal tellurides. MoTe₂ undergoes a structural phase transition from the centrosymmetric monoclinic 1T' phase to the inversion-breaking T_d phase at low temperatures and is sensitive to the sample's RRR. 80 It exhibits temperature-dependent topological phase transition between topological phase I (8 Weyl points) and topological phase II (4 Weyl points) at higher RRR(>100). Higher RRR values correlate with stabilization of the T_d phase and, consequently, the appearance of Weyl semimetal behavior. In contrast, WTe₂ exhibits a temperature-independent T_d phase, remaining structurally and topologically stable over a wide range. However, the associated Fermi arc surface states in WTe2 are typically shorter and less pronounced than those in MoTe₂.⁸¹ Fedchenko et al.⁶² demonstrated that a small substitution of W into $MoTe_2$ ($Mo_{0.91}W_{0.09}Te_2$) (RRR = 8) can stabilize the $T_{\rm d}$ phase around 170 K and reveal the

presence of Fermi arc surface states. Their theoretical analysis attributed these surface states to contributions from Mo-d orbitals, confirming their role in shaping the surface topological features. The T_d phase, unlike the 1T' phase, displays crystal inversion symmetry breaking, leading to significant band splitting in the electronic structure except at time-reversal invariant points. In addition, the $T_{\rm d}$ phase exhibits a large, nonsaturating magnetoresistance, a hallmark of Weyl semimetal behavior, in which low-energy quasiparticles behave as Weyl Fermions. Our findings point toward the rich tunability in Mo_xW_{1-x}Te₂ alloys, particularly in the intermediate range of x = 0.1 to 0.5, which bridges the contrasting behaviors of pure MoTe₂ and WTe₂. In particular, Mo_{0.3}W_{0.7}Te₂ exhibits enhanced $T_{\rm d}$ phase stability at room temperature. The substantial Mo-d orbital contribution may enhance the topologically protected Fermi arc surface states. Based on both experimental trends and theoretical predictions, this composition stands as a strong candidate for realizing robust Fermi arc surface states and Weyl semimetal phases under ambient conditions, offering a promising platform for topological quantum devices.

In addition, these findings underscore the importance of characterizing and stabilizing the $T_{\rm d}$ phase, which emerges as a favorable structural phase for achieving enhanced MR through its superior crystal quality and transport characteristics. In addition, the introduction of Mo predominantly alters the scattering mechanism, disrupting the balance between phonon and impurity scattering. As the Mo content increases, replacing W, it significantly modifies carrier dynamics at elevated temperatures by introducing additional scattering centers and altering the electronic band structure. These findings highlight the role of Mo substitution in tuning the transport properties of the material, making it a critical factor in optimizing performance.

CONCLUSIONS

We synthesized the stoichiometric type II Weyl semimetal candidate $Mo_xW_{1-x}Te_2$ (x = 0.1 - 0.5) and investigated the origin of magnetoresistance (MR) in relation to structural modifications. XRD and Raman spectroscopy confirmed that all samples exhibit an intermediate phase between T_d and 1T'. Substituting Mo for W induced lattice contraction and reduced crystal quality, as indicated by poor residual resistivity ratio (RRR) values. These structural changes suppressed MR due to reduced crystal quality, increased electron-hole concentration asymmetry, and decreased carrier mobility. Importantly, the structural modifications associated with the T_d phase also influence transport properties, creating anomalies such as that observed at x = 0.3. At this configuration, the T_d phase is more stable, resulting in enhanced MR and improved crystal quality. These results highlight the significant role of structural properties, particularly the stabilization of the T_d phase, in enhancing the MR. This finding underscores that while electron-hole asymmetry, high mobility, and RRR values are important, structural modulation also plays a critical role in the transport mechanism of Weyl semimetals. Future work will focus on investigating the electronic band structure of Mo_xW_{1-x}Te₂ to understand the evolution of the MR further and study the topologically protected Fermi arc surface states. These insights provide a deeper understanding of the interplay between structure and electronic properties in Weyl semimetals, offering implications for their applications in spintronics and quantum materials research.

ASSOCIATED CONTENT

Supporting Information

The Supporting Information is available free of charge at https://pubs.acs.org/doi/10.1021/acs.jpcc.5c01464.

Tables summerizing the parameters of Le Bail model fitting of the XRD data, observed values of characteristic temperatures $T_{\rm i}$ and $T_{\rm m}$, fitting parameters obtained from the analysis of the two-band model and the linear fit parameters of Kohler scaling, graphics showing the SEM elemental mapping and corresponding EDS spectra, and XRD data fitted with the Le Bail model (PDF)

AUTHOR INFORMATION

Corresponding Author

Sanjoy Kr Mahatha — UGC-DAE Consortium for Scientific Research, Indore 452001, India; ⊚ orcid.org/0000-0002-5394-6911; Email: sanjoymahatha@gmail.com

Authors

Sambit Choudhury – UGC-DAE Consortium for Scientific Research, Indore 452001, India

Shailesh Kalal — Thin Film Physics Division, Department of Physics Chemistry and Biology (IFM), Linköping University, SE-581 83 Linköping, Sweden; orcid.org/0000-0003-4864-596X

Rajesh Kumar Ulaganathan — Centre for Nanotechnology, Indian Institute of Technology Roorkee, Roorkee 247667, India; Occid.org/0000-0001-8886-6332

Raman Sankar — Institute of Physics, Academia Sinica, Taipei 11529, Taiwan; oorcid.org/0000-0003-4702-2517

Complete contact information is available at: https://pubs.acs.org/10.1021/acs.jpcc.5c01464

Notes

The authors declare no competing financial interest.

ACKNOWLEDGMENTS

The authors thank Dr. M. P. Saravanan, Dr. V. R. Reddy, and Dr. V. G. Sathe for magnetoresistance, XRD, and Raman studies, respectively. Synchrotron XRD studies were performed at the PETRA III light source of DESY, a member of the Helmholtz Association (HGF). We would like to thank the supporting beamline staff for their assistance at beamline P24. The financial support provided by the Department of Science and Technology (Government of India) within the framework of the India@DESY collaboration is gratefully acknowledged. R.S. acknowledges the financial support provided by the Ministry of Science and Technology in Taiwan under Project No. NSTC-113-2124-M-001-003 and No. NSTC-113-2112M001-045-MY3, as well as support from Academia Sinica for the budget of AS-iMATE11412. R.K.U. would like to acknowledge the IITR for the Faculty Initiation Grant (FIG-101068).

REFERENCES

- (1) Liang, T.; Gibson, Q.; Ali, M. N.; Liu, M.; Cava, R.; Ong, N. Ultrahigh mobility and giant magnetoresistance in the Dirac semimetal Cd3As2. *Nat. Mater.* **2015**, *14*, 280–284.
- (2) Shekhar, C.; Nayak, A. K.; Sun, Y.; Schmidt, M.; Nicklas, M.; Leermakers, I.; Zeitler, U.; Skourski, Y.; Wosnitza, J.; Liu, Z.; et al. Extremely large magnetoresistance and ultrahigh mobility in the

- topological Weyl semimetal candidate NbP. Nat. Phys. 2015, 11, 645-649.
- (3) Wang, Y.-Y.; Yu, Q.-H.; Guo, P.-J.; Liu, K.; Xia, T.-L. Resistivity plateau and extremely large magnetoresistance in NbAs₂ and TaAs₂. *Phys. Rev. B* **2016**, *94*, No. 041103.
- (4) Gao, W.; Hao, N.; Zheng, F.-W.; Ning, W.; Wu, M.; Zhu, X.; Zheng, G.; Zhang, J.; Lu, J.; Zhang, H.; et al. Extremely Large Magnetoresistance in a Topological Semimetal Candidate Pyrite *PtBi*₂. *Phys. Rev. Lett.* **2017**, *118*, No. 256601.
- (5) Xu, J.; Ghimire, N. J.; Jiang, J. S.; Xiao, Z. L.; Botana, A. S.; Wang, Y. L.; Hao, Y.; Pearson, J. E.; Kwok, W. K. Origin of the extremely large magnetoresistance in the semimetal YSb. *Phys. Rev. B* **2017**, *96*, No. 075159.
- (6) Wang, X.; Du, Y.; Dou, S.; Zhang, C. Room Temperature Giant and Linear Magnetoresistance in Topological Insulator Bi₂Te₃ Nanosheets. *Phys. Rev. Lett.* **2012**, *108*, No. 266806.
- (7) Lou, R.; Xu, Y. F.; Zhao, L.-X.; Han, Z.-Q.; Guo, P.-J.; Li, M.; Wang, J.-C.; Fu, B.-B.; Liu, Z.-H.; Huang, Y.-B.; et al. Observation of open-orbit Fermi surface topology in the extremely large magnetoresistance semimetal MoAs₂. *Phys. Rev. B* **2017**, *96*, No. 241106.
- (8) Pavlosiuk, O.; Kaczorowski, D. Galvanomagnetic properties of the putative type-II Dirac semimetal PtTe2. Sci. Rep. 2018, 8, 11297.
- (9) Wang, Y.; Zhang, J.; Zhu, W.; Zou, Y.; Xi, C.; Ma, L.; Han, T.; Yang, J.; Wang, J.; Xu, J.; et al. De Hass-van Alphen and magnetoresistance reveal predominantly single-band transport behavior in PdTe2. Sci. Rep. 2016, 6, No. 31554.
- (10) Tao, Y.; Schneeloch, J. A.; Duan, C.; Matsuda, M.; Dissanayake, S. E.; Aczel, A. A.; Fernandez-Baca, J. A.; Ye, F.; Louca, D. Appearance of a T_d^* phase across the T_d –1T' phase boundary in the Weyl semimetal MoTe₂. *Phys. Rev. B* **2019**, *100*, No. 100101.
- (11) Tao, Y.; Schneeloch, J. A.; Aczel, A. A.; Louca, D. $T_{\rm d}$ to 1T' structural phase transition in the WTe₂ Weyl semimetal. *Phys. Rev. B* **2020**, *102*, No. 060103.
- (12) Ali, M. N.; Xiong, J.; Flynn, S.; Tao, J.; Gibson, Q. D.; Schoop, L. M.; Liang, T.; Haldolaarachchige, N.; Hirschberger, M.; Ong, N. P.; et al. Large, non-saturating magnetoresistance in WTe2. *Nature* **2014**, *514*, 205–208.
- (13) Ali, M. N.; Schoop, L.; Xiong, J.; Flynn, S.; Gibson, Q.; Hirschberger, M.; Ong, N. P.; Cava, R. J. Correlation of crystal quality and extreme magnetoresistance of WTe2. *Europhys. Lett.* **2015**, *110*, 67002.
- (14) Cai, P. L.; Hu, J.; He, L. P.; Pan, J.; Hong, X. C.; Zhang, Z.; Zhang, J.; Wei, J.; Mao, Z. Q.; Li, S. Y. Drastic Pressure Effect on the Extremely Large Magnetoresistance in WTe₂: Quantum Oscillation Study. *Phys. Rev. Lett.* **2015**, *115*, No. 057202.
- (15) Luo, X.; Fang, C.; Wan, C.; Cai, J.; Liu, Y.; Han, X.; Lu, Z.; Shi, W.; Xiong, R.; Zeng, Z. Magnetoresistance and Hall resistivity of semimetal WTe2 ultrathin flakes. *Nanotechnology* **2017**, *28*, 145704.
- (16) Kong, W. D.; Wu, S. F.; Richard, P.; Lian, C. S.; Wang, J. T.; Yang, C. L.; Shi, Y. G.; Ding, H. Raman scattering investigation of large positive magnetoresistance material WTe2. *Appl. Phys. Lett.* **2015**, *106*, No. 081906.
- (17) Li, S.; Lei, F.-c.; Peng, X.; Wang, R.-q.; Xie, J.-f.; Wu, Y.-p.; Li, D.-s. Synthesis of semiconducting 2H-phase WTe2 nanosheets with large positive magnetoresistance. *Inorg. Chem.* **2020**, *59*, 11935–11939.
- (18) Lv, H. Y.; Lu, W. J.; Shao, D. F.; Liu, Y.; Tan, S. G.; Sun, Y. P. Perfect charge compensation in WTe2 for the extraordinary magnetoresistance: From bulk to monolayer. *Europhys. Lett.* **2015**, 110, 37004.
- (19) Pletikosić, I.; Ali, M. N.; Fedorov, A. V.; Cava, R. J.; Valla, T. Electronic Structure Basis for the Extraordinary Magnetoresistance in WTe₂. *Phys. Rev. Lett.* **2014**, *113*, No. 216601.
- (20) Tsumura, K.; Yano, R.; Kashiwaya, H.; Koyanagi, M.; Masubuchi, S.; Machida, T.; Namiki, H.; Sasagawa, T.; Kashiwaya, S. Extremely large magnetoresistance in a high-quality WTe2 grown by flux method. *Journal of Physics: Conference Series* **2018**, 969, No. 012134.

- (21) Wang, Y. L.; Thoutam, L. R.; Xiao, Z. L.; Hu, J.; Das, S.; Mao, Z. Q.; Wei, J.; Divan, R.; Luican-Mayer, A.; Crabtree, G. W.; et al. Origin of the turn-on temperature behavior in WTe₂. *Phys. Rev. B* **2015**, *92*, No. 180402.
- (22) Zhao, Y.; Liu, H.; Yan, J.; An, W.; Liu, J.; Zhang, X.; Wang, H.; Liu, Y.; Jiang, H.; Li, Q.; et al. Anisotropic magnetotransport and exotic longitudinal linear magnetoresistance in WTe₂ crystals. *Phys. Rev. B* **2015**, 92, No. 041104.
- (23) Zhu, Z.; Lin, X.; Liu, J.; Fauqué, B.; Tao, Q.; Yang, C.; Shi, Y.; Behnia, K. Quantum Oscillations, Thermoelectric Coefficients, and the Fermi Surface of Semimetallic WTe₂. *Phys. Rev. Lett.* **2015**, *114*, No. 176601.
- (24) Keum, D. H.; Cho, S.; Kim, J. H.; Choe, D.-H.; Sung, H.-J.; Kan, M.; Kang, H.; Hwang, J.-Y.; Kim, S. W.; Yang, H.; et al. Bandgap opening in few-layered monoclinic MoTe2. *Nat. Phys.* **2015**, *11*, 482–486.
- (25) Thirupathaiah, S.; Jha, R.; Pal, B.; Matias, J. S.; Das, P. K.; Sivakumar, P. K.; Vobornik, I.; Plumb, N. C.; Shi, M.; Ribeiro, R. A.; et al. MoTe₂: An uncompensated semimetal with extremely large magnetoresistance. *Phys. Rev. B* **2017**, *95*, No. 241105.
- (26) Yang, J.; Colen, J.; Liu, J.; Nguyen, M. C.; Chern, G. w.; Louca, D. Elastic and electronic tuning of magnetoresistance in MoTe2. *Sci. Adv.* **2017**, *3*, No. eaao4949.
- (27) Chen, F. C.; Lv, H. Y.; Luo, X.; Lu, W. J.; Pei, Q. L.; Lin, G. T.; Han, Y. Y.; Zhu, X. B.; Song, W. H.; Sun, Y. P. Extremely large magnetoresistance in the type-II Weyl semimetal MoTe₂. *Phys. Rev. B* **2016**, *94*, No. 235154.
- (28) Zhong, S.; Tiwari, A.; Nichols, G.; Chen, F.; Luo, X.; Sun, Y.; Tsen, A. W. Origin of magnetoresistance suppression in thin γ -MoTe₂. *Phys. Rev. B* **2018**, 97, No. 241409.
- (29) Pei, Q. L.; Luo, X.; Chen, F. C.; Lv, H. Y.; Sun, Y.; Lu, W. J.; Tong, P.; Sheng, Z. G.; Han, Y. Y.; Song, W. H.; Zhu, X. B.; Sun, Y. P.; et al. Mobility spectrum analytical approach for the type-II Weyl semimetal Td-MoTe2. *Appl. Phys. Lett.* **2018**, *112*, No. 072401.
- (30) Lee, S.; Jang, J.; Kim, S.-I.; Jung, S.-G.; Kim, J.; Cho, S.; Kim, S. W.; Rhee, J. Y.; Park, K.-S.; Park, T. Origin of extremely large magnetoresistance in the candidate type-II Weyl semimetal MoTe_{2-x}. *Sci. Rep.* **2018**, *8*, 13937.
- (31) Brown, B. E. The crystal structures of WTe2 and high-temperature MoTe2. Acta Crystallogr. 1966, 20, 268–274.
- (32) Dawson, W. G.; Bullett, D. W. Electronic structure and crystallography of MoTe2 and WTe2. *Journal of Physics C: Solid State Physics* **1987**, 20, 6159.
- (33) Mar, A.; Jobic, S.; Ibers, J. A. Metal-metal vs tellurium-tellurium bonding in WTe2 and its ternary variants TaIrTe4 and NbIrTe4. *J. Am. Chem. Soc.* **1992**, *114*, 8963–8971.
- (34) Qian, X.; Liu, J.; Fu, L.; Li, J. Quantum spin Hall effect in two-dimensional transition metal dichalcogenides. *Science* **2014**, *346*, 1344–1347.
- (35) Empante, T. A.; Zhou, Y.; Klee, V.; Nguyen, A. E.; Lu, I.-H.; Valentin, M. D.; Naghibi Alvillar, S. A.; Preciado, E.; Berges, A. J.; Merida, C. S.; et al. Chemical vapor deposition growth of few-layer MoTe2 in the 2H, 1T, and 1T phases: tunable properties of MoTe2 films. *ACS Nano* **2017**, *11*, 900–905.
- (36) So, C.; Zhang, H.; Wang, Y.; Ye, M.; Pan, Y.; Quhe, R.; Li, J. Z.; Zhang, X.; Zhou, Y.; Lu, J. A computational study of monolayer hexagonal WTe2 to metal interfaces. *phys. status solidi* (b) **2017**, 254, No. 1600837.
- (37) Woldesenbet, M.; Debelo, N.; Woldemariam, M. Structural, Electronic, Dynamic, and Optical Properties of 2D Monolayer Tungsten Telluride (2H-WTe2) under Small Biaxial Strain Using Density Functional Theory (DFT and DFT+ U). *Adv. Condens. Matter Phys.* **2023**, 2023, No. 3179210.
- (38) Dong, X.; Li, H.; Chen, T.; Xu, L.; Zhou, G. Defects-/doping-driven modulation of the electronic and magnetic properties of 2H-and Td-phase WTe2 monolayers: A first-principle study. *Materials Science in Semiconductor Processing* **2022**, *143*, No. 106537.
- (39) Xu, X.; Pan, Y.; Liu, S.; Han, B.; Gu, P.; Li, S.; Xu, W.; Peng, Y.; Han, Z.; Chen, J.; et al. Seeded 2D epitaxy of large-area single-crystal

- films of the van der Waals semiconductor 2H MoTe₂. Science 2021, 372, 195–200.
- (40) Pan, Y.; Song, Y.; Wang, Q.; Wang, T.; Li, Y.; Xu, W.; Ye, Y. Direct Multitier Synthesis of Two-Dimensional Semiconductor 2H-MoTe2. ACS Appl. Electron. Mater. 2022, 4, 5733–5738.
- (41) Lee, C.-H.; Silva, E. C.; Calderin, L.; Nguyen, M. A. T.; Hollander, M. J.; Bersch, B.; Mallouk, T. E.; Robinson, J. A. Tungsten Ditelluride: a layered semimetal. *Sci. Rep.* **2015**, *5*, No. 10013.
- (42) Jana, M. K.; Singh, A.; Late, D. J.; Rajamathi, C. R.; Biswas, K.; Felser, C.; Waghmare, U. V.; Rao, C. N. R. A combined experimental and theoretical study of the structural, electronic and vibrational properties of bulk and few-layer Td-WTe2. *J. Phys.: Condens. Matter* 2015, 27, 285401.
- (43) Das, P. K.; Di Sante, D.; Cilento, F.; Bigi, C.; Kopic, D.; Soranzio, D.; Sterzi, A.; Krieger, J. A.; Vobornik, I.; Fujii, J.; Okuda, T.; Strocov, V. N.; Breese, M. B. H.; Parmigiani, F.; Rossi, G.; Picozzi, S.; Thomale, R.; Sangiovanni, G.; Cava, R. J.; Panaccione, G.; et al. Electronic properties of candidate type-II Weyl semimetal WTe2. A review perspective. *Electron. Struct.* 2019, 1, No. 014003.
- (44) Augustin, J.; Eyert, V.; Böker, T.; Frentrup, W.; Dwelk, H.; Janowitz, C.; Manzke, R. Electronic band structure of the layered compound Td–WTe₂. *Phys. Rev. B* **2000**, *62*, 10812–10823.
- (45) Zheng, F.; Cai, C.; Ge, S.; Zhang, X.; Liu, X.; Lu, H.; Zhang, Y.; Qiu, J.; Taniguchi, T.; Watanabe, K.; et al. On the Quantum Spin Hall Gap of Monolayer 1T-WTe2. *Adv. Mater.* **2016**, *28*, 4845–4851.
- (46) Tang, S.; Zhang, C.; Wong, D.; Pedramrazi, Z.; Tsai, H.-Z.; Jia, C.; Moritz, B.; Claassen, M.; Ryu, H.; Kahn, S.; et al. Quantum spin Hall state in monolayer 1T'-WTe2. *Nat. Phys.* **2017**, *13*, 683–687.
- (47) Niu, R.; Zhu, W. K. Materials and possible mechanisms of extremely large magnetoresistance: a review. *J. Phys.: Condens. Matter* **2022**, *34*, 113001.
- (48) Marchenkov, V.; Perevalova Domozhirova, A.; Naumov, S.; Podgornykh, S.; Marchenkova, E.; Chistyakov, V.; Huang, J. Peculiarities of electronic transport in WTe2 single crystal. *J. Magn. Magn. Mater.* **2022**, 549, No. 168985.
- (49) Perevalova, A.; Naumov, S.; Podgornykh, S.; Chistyakov, V.; Marchenkova, E.; Fominykh, B.; Marchenkov, V. Kinetic Properties of a Topological Semimetal WTe2 Single Crystal. *Physics of Metals and Metallography* **2022**, *123*, 1061–1067.
- (50) Pei, Q. L.; Meng, W. J.; Luo, X.; Lv, H. Y.; Chen, F. C.; Lu, W. J.; Han, Y. Y.; Tong, P.; Song, W. H.; Hou, Y. B.; et al. Origin of the turn-on phenomenon in T_d -MoTe₂. *Phys. Rev. B* **2017**, 96, No. 075132.
- (51) Fu, D.; Pan, X.; Bai, Z.; Fei, F.; Umana-Membreno, G. A.; Song, H.; Wang, X.; Wang, B.; Song, F. Tuning the electrical transport of type II Weyl semimetal WTe2 nanodevices by Mo doping. *Nanotechnology* **2018**, *29*, 135705.
- (52) Xiang, F.-X.; Veldhorst, M.; Dou, S.-X.; Wang, X.-L. Multiple Fermi pockets revealed by Shubnikov-de Haas oscillations in WTe2. *Europhys. Lett.* **2015**, *112*, 37009.
- (53) Barua, S.; Lees, M. R.; Balakrishnan, G.; Goddard, P. A. Quantum oscillation study of the large magnetoresistance in Mo substituted WTe₂ single crystals. *Phys. Rev. B* **2024**, *110*, No. 155113.
- (54) Luo, X.; Chen, F. C.; Zhang, J. L.; Pei, Q. L.; Lin, G. T.; Lu, W. J.; Han, Y. Y.; Xi, C. Y.; Song, W. H.; Sun, Y. P. Td-MoTe2: A possible topological superconductor. *Appl. Phys. Lett.* **2016**, *109*, 102601.
- (55) Thirupathaiah, S.; Jha, R.; Pal, B.; Matias, J. S.; Das, P. K.; Vobornik, I.; Ribeiro, R. A.; Sarma, D. D. Temperature-independent band structure of WTe₂ as observed from angle-resolved photoemission spectroscopy. *Phys. Rev. B* **2017**, *96*, No. 165149.
- (56) Rhodes, D.; Das, S.; Zhang, Q. R.; Zeng, B.; Pradhan, N. R.; Kikugawa, N.; Manousakis, E.; Balicas, L. Role of spin-orbit coupling and evolution of the electronic structure of WTe₂ under an external magnetic field. *Phys. Rev. B* **2015**, *92* (92), No. 125152.
- (57) Jiang, J.; Tang, F.; Pan, X. C.; Liu, H. M.; Niu, X. H.; Wang, Y. X.; Xu, D. F.; Yang, H. F.; Xie, B. P.; Song, F. Q.; et al. Signature of Strong Spin-Orbital Coupling in the Large Nonsaturating Magnetoresistance Material WTe₂. *Phys. Rev. Lett.* **2015**, *115*, No. 166601.

- (58) Wang, Y.; Wang, K.; Reutt-Robey, J.; Paglione, J.; Fuhrer, M. S. Breakdown of compensation and persistence of nonsaturating magnetoresistance in gated *WTe*₂ thin flakes. *Phys. Rev. B* **2016**, 93, No. 121108.
- (59) Lv, Y.-Y.; Zhang, B.; Li, X.; Pang, B.; Zhang, F.; Lin, D.-J.; Zhou, J.; Yao, S.; Chen, Y.; Zhang, S.-T.; et al. Dramatically decreased magnetoresistance in non-stoichiometric WTe2 crystals. *Sci. Rep.* **2016**, *6*, No. 26903.
- (60) Chang, T.-R.; Xu, S.-Y.; Chang, G.; Lee, C.-C.; Huang, S.-M.; Wang, B.; Bian, G.; Zheng, H.; Sanchez, D. S.; Belopolski, I.; et al. Prediction of an arc-tunable Weyl Fermion metallic state in MoxW1-xTe2. *Nat. Commun.* **2016**, *7*, No. 10639.
- (61) Deng, Y.; Li, P.; Zhu, C.; Zhou, J.; Wang, X.; Cui, J.; Yang, X.; Tao, L.; Zeng, Q.; Duan, R.; et al. Controlled Synthesis of MoxW1–xTe2 Atomic Layers with Emergent Quantum States. *ACS Nano* **2021**, *15*, 11526–11534.
- (62) Fedchenko, O.; Diekmann, F.; Russmann, P.; Kallmayer, M.; Odenbreit, L.; Souliou, S.; Frachet, M.; Winkelmann, A.; Merz, M.; Chernov, S. et al. Doping-Induced Electronic and Structural Phase Transition in the Bulk Weyl Semimetal Mo1-xWxTe2. arXiv preprint arXiv:2310.10593 2023.
- (63) Dahal, R.; Deng, L. Z.; Poudel, N.; Gooch, M.; Wu, Z.; Wu, H. C.; Yang, H. D.; Chang, C. K.; Chu, C. W. Tunable structural phase transition and superconductivity in the Weyl semimetal Mo_{1-x} W_xTe_2 . *Phys. Rev. B* **2020**, *101*, No. 140505.
- (64) Lee, H. H.; Lim, E.; Kang, S.; Eshete, Y. A.; Won, D.; Lee, Y.; Yeong Jeong, J.; Yang, H.; Chiang, C.-Y.; Cho, S. Local phase transition at crack edges of Mo1xWxTe2 polymorphs. *Appl. Surf. Sci.* **2022**, *596*, No. 153503.
- (65) Lv, Y.-Y.; Cao, L.; Li, X.; Zhang, B.-B.; Wang, K.; Pang, B.; Ma, L.; Lin, D.; Yao, S.-H.; Zhou, J.; et al. Composition and temperature-dependent phase transition in miscible Mo1- x W x Te2 single crystals. Sci. Rep. 2017, 7, No. 44587.
- (66) Oliver, S. M.; Beams, R.; Krylyuk, S.; Kalish, I.; Singh, A. K.; Bruma, A.; Tavazza, F.; Joshi, J.; Stone, I. R.; Stranick, S. J.; et al. The structural phases and vibrational properties of Mo1xWxTe2 alloys. 2D *Materials* **2017**, *4*, No. 045008.
- (67) Schneeloch, J. A.; Tao, Y.; Duan, C.; Matsuda, M.; Aczel, A. A.; Fernandez-Baca, J. A.; Xu, G.; Neuefeind, J. C.; Yang, J.; Louca, D. Evolution of the structural transition in $Mo_{1-x}W_xTe_2$. *Phys. Rev. B* **2020**, *102*, No. 054105.
- (68) Rhodes, D.; Chenet, D. A.; Janicek, B. E.; Nyby, C.; Lin, Y.; Jin, W.; Edelberg, D.; Mannebach, E.; Finney, N.; Antony, A.; et al. Engineering the Structural and Electronic Phases of MoTe2 through W Substitution. *Nano Lett.* **2017**, *17*, 1616–1622.
- (69) Ma, X.; Guo, P.; Yi, C.; Yu, Q.; Zhang, A.; Ji, J.; Tian, Y.; Jin, F.; Wang, Y.; Liu, K.; et al. Raman scattering in the transition-metal dichalcogenides of $1T'-{\rm MoTe}_2$, $T_d-{\rm MoTe}_2$, and $T_d-{\rm WTe}_2$. *Phys. Rev. B* **2016**, 94, No. 214105.
- (70) Nagpal, V.; Jat, K.; Patnaik, S. Magnetoresistance and scaling laws in type-II Weyl semimetal WP2. *Physica B: Condensed Matter* **2021**, *616*, No. 413062.
- (71) Wang, A.; Graf, D.; Stein, A.; Liu, Y.; Yin, W.; Petrovic, C. Magnetotransport properties of MoP₂. *Phys. Rev. B* **2017**, 96, No. 195107.
- (72) Khveshchenko, D. V. Magnetic-Field-Induced Insulating Behavior in Highly Oriented Pyrolitic Graphite. *Phys. Rev. Lett.* **2001**, *87*, No. 206401.
- (73) Kopelevich, Y.; Torres, J. H. S.; da Silva, R. R.; Mrowka, F.; Kempa, H.; Esquinazi, P. Reentrant Metallic Behavior of Graphite in the Quantum Limit. *Phys. Rev. Lett.* **2003**, *90*, No. 156402.
- (74) Kopelevich, Y.; Pantoja, J. C. M.; da Silva, R. R.; Moehlecke, S. Universal magnetic-field-driven metal-insulator-metal transformations in graphite and bismuth. *Phys. Rev. B* **2006**, *73*, No. 165128.
- (75) Pan, X.-C.; Chen, X.; Liu, H.; Feng, Y.; Wei, Z.; Zhou, Y.; Chi, Z.; Pi, L.; Yen, F.; Song, F.; et al. Pressure-driven dome-shaped superconductivity and electronic structural evolution in tungsten ditelluride. *Nat. Commun.* **2015**, *6*, 7805.

- (76) Zhang, L.; Liang, Q.; Xiong, Y.; Zhang, B.; Gao, L.; Li, H.; Chen, Y. B.; Zhou, J.; Zhang, S.-T.; Gu, Z.-B.; et al. Tunable semimetallic state in compressive-strained SrIrO₃ films revealed by transport behavior. *Phys. Rev. B* **2015**, *91*, No. 035110.
- (77) Jo, N. H.; Wu, Y.; Wang, L.-L.; Orth, P. P.; Downing, S. S.; Manni, S.; Mou, D.; Johnson, D. D.; Kaminski, A.; Bud'ko, S. L.; et al. Extremely large magnetoresistance and Kohler's rule in PdSn₄: A complete study of thermodynamic, transport, and band-structure properties. *Phys. Rev. B* **2017**, *96*, No. 165145.
- (78) Du, J.; Lou, Z.; Zhang, S.; Zhou, Y.; Xu, B.; Chen, Q.; Tang, Y.; Chen, S.; Chen, H.; Zhu, Q.; et al. Extremely large magnetoresistance in the topologically trivial semimetal α –WP $_2$. Phys. Rev. B **2018**, 97, No. 245101.
- (79) Akhanda, M. S.; Krylyuk, S.; Dickie, D. A.; Davydov, A. V.; Han, F.; Li, M.; Zebarjadi, M. Phase-transition-induced thermal hysteresis in Type-II weyl semimetals MoTe2 and Mo1xWxTe2. *Materials Today Physics* **2022**, *29*, No. 100918.
- (80) Zhang, A.; Ma, X.; Liu, C.; Lou, R.; Wang, Y.; Yu, Q.; Wang, Y.; Xia, T.-L.; Wang, S.; Zhang, L.; et al. Topological phase transition between distinct Weyl semimetal states in MoTe₂. *Phys. Rev. B* **2019**, 100, No. 201107.
- (81) Belopolski, I.; Sanchez, D. S.; Ishida, Y.; Pan, X.; Yu, P.; Xu, S.-Y.; Chang, G.; Chang, T.-R.; Zheng, H.; Alidoust, N.; et al. Discovery of a new type of topological Weyl fermion semimetal state in MoxW1-xTe2. *Nat. Commun.* **2016**, *7*, No. 13643.